nature communications

Article

https://doi.org/10.1038/s41467-025-68278-z

Refrigeration down to 0.16 K using a frustrated magnet $Gd_2B_2MoO_9$

Received: 9 July 2025

Accepted: 24 December 2025

Yikun Zhang[1], Yingzhe Na[1], Xinyang Liu[2], Junsen Xiang[2], Fengying Chen[1], Hai-Feng Li[3], Peijie Sun[2], Shengqiang Zhou[4], Xuefeng Zhang[1] & Lingwei Li[1]

Magnetic refrigeration, utilizing the magnetocaloric effect in solid-state magnets, has emerged as a promising cooling technology. The development of practical ultra-low-temperature magnetic refrigeration applications has been limited by the absence of high-performance magnetic refrigerants. Herein, we provide a frustrated Gadolinium-dominated magnet, $Gd_2B_2MoO_9$ oxide, which exhibits remarkable ultra-low temperature magnetocaloric performances. The maximum magnetic entropy changes reach 13.3 (76.6), 33.7 (194.0) and 45.1 (259.8) J/kgK (mJ/cm^{3}K) under relatively low magnetic field changes of 0-1, 0-2 and 0-3 T, respectively. A minimum temperature of 0.16 K has been achieved by a custom-built quasi-adiabatic demagnetization apparatus. These magnetocaloric performances surpass those of the commercial ultra-low temperature magnetic refrigerant $Gd_3Ga_5O_{12}$ and outperform most of recently reported materials. Combined with its relatively high density and environmental stability, the geometrically frustrated $Gd_2B_2MoO_9$ oxide is established as an attractive ultra-low temperature magnetic refrigerant.

Ultra-low temperature conditions are crucial for various cutting-edge technological and scientific fields, such as space exploration, superconductor science, quantum physics and technology[1–7]. However, current refrigeration technologies rely heavily on liquid He, which is a depleting resource and increasingly difficult to obtain[8]. Thus, there is an urgent need to explore alternative cooling methods that can operate without liquid He[8–11]. Magnetic refrigeration (MR)[11–13], which utilizes the magnetocaloric (MC) effect in solid-state magnets, offers an excellent alternative. The MC effect, an inherent magneto-thermal property of magnets[11–13], can be primarily quantified by the magnetic entropy change ($-\Delta S_M$) under certain magnetic field variations ($\Delta\mu_0H$). Ultra-low temperature magnetic refrigerants are generally effective only close to and slightly above their magnetic ordering temperatures (T_M). Historically, the low-temperature MR concept was first demonstrated experimentally by adiabatic demagnetization refrigeration (ADR) in the early 1930s[14–16]. Early ultra-low temperature ADR mainly utilized water-containing salts, such as $Ce_2Mg_3(NO_3)_{12}{\cdot}24H_2O$, $Gd_2(SO_4)_3{\cdot}8H_2O$, $CrK(SO_4)_2{\cdot}12H_2O$, and $Fe(SO_4)_2(NH_4){\cdot}12H_2O$[15–18], in which the magnetic ions are separated by water molecules, resulting in ultra-low T_M. However, these materials exhibit poor environmental stability and low density of magnetic ions, which limits their widespread applications.

Over the past thirty years, systematic MC characterization has been undertaken in some rare-earth (*RE*)-dominated magnetic solids[19–28], and some trivalent Gadolinium (Gd)- and divalent Europium (Eu)-dominated magnets with low T_M are found to demonstrate notable low-temperature MC performances[21–26]. This is related to the high-spin-only ground state of Gd^{3+} and Eu^{2+} ions ($J = S = 7/2$), which results in low magnetic anisotropy and large magnetic entropy. However, high-performing magnetic refrigerants that are effective at ultra-low temperature below 1 K are still rare, since a higher density of magnetic ions usually results in stronger exchange interactions and

---

[1]Key Laboratory of Novel Materials for Sensor of Zhejiang Province, Hangzhou Dianzi University, Hangzhou, China. [2]Beijing National Laboratory for Condensed Matter Physics, Institute of Physics, Chinese Academy of Science, Beijing, China. [3]Institute of Applied Physics and Materials Engineering, University of Macau, Avenida da Universidade, Taipa, Macao SAR, China. [4]Helmholtz-Zentrum Dresden-Rossendorf, Institute of Ion Beam Physics and Materials Research, Dresden, Germany. e-mail: lingwei@hdu.edu.cn

thus higher T_M[19–24]. Currently, the commercialized ultra-low temperature magnetic refrigerant is gadolinium gallium garnet ($Gd_3Ga_5O_{12}$), which exhibits prominent MC performances with $-\Delta S_M^{max}$ of 38.4 J/kgK ($\Delta\mu_0 H = 0–7$ T) as well as high density (7.09 g/cm^3)[27,28].

We herein shifted our attention to geometrically frustrated (GF) magnets, which present a diverse class of magnets with peculiar cryogenic physical phenomenon such as large ground state degeneracy, unconventional phase transitions, and unusual quantum spin states[29–35]. The magnetic ions in GF systems are generally arranged in nearly equilateral triangle lattices, which prevents the nearest neighbor exchange interactions from being satisfied simultaneously[29–31]. It has also been theoretically proposed around three decades ago that magnetic frustration can enhance low-temperature MC response by suppressing T_M with high magnetic ion density and thus maintaining large magnetic entropy at low-temperatures[33]. As stated above, the $Gd_3Ga_5O_{12}$ oxide[27,28], the only commercialized ultra-low temperature magnetic refrigerant up to present, shows a typical three corner-sharing garnet type GF structure. Koskelo et al. have provided a comparative study of the MC effects in several Gd-dominated magnets with different GF lattices, and they found that the lattice geometry and degree of magnetic frustration play vital roles in their low-temperature MC performances[34]. We have recently unveiled the MC properties of pyrochlore-type GF structured $Gd_2Ti_2O_7$ oxide with strong magnetic frustrations, and a moderate MC performance with $-\Delta S_M^{max}$ of 15.43 J/kgK under $\Delta\mu_0 H$ of 0–5 T was realized[35]. Nonetheless, the reported GF magnets with prominent ultra-low temperature MC performances remain quite limited due to the lack of material systems with a high density of magnetic ions and a suitable degree of magnetic frustration.

In this work, we present a Gd-dominated GF magnet with moderate magnetic frustration, $Gd_2B_2MoO_9$ oxide, possessing excellent ultra-low temperature MC performances. This material adopts an antiferromagnetic semiconductor ground state and exhibits remarkable maximum magnetic entropy changes of 13.3 (76.6) and 33.7 (194.0) J/kgK (mJ/cm^{3}K) under low magnetic field changes of 0–1 and 0–2 T, respectively. Utilizing a custom-built quasi-adiabatic demagnetization apparatus, we successfully achieved a minimum temperature of 0.16 K, which is low enough for solid-state quantum computers[36,37]. These MC performances are significantly better than those of the commercial ultra-low temperature magnetic refrigerant $Gd_3Ga_5O_{12}$ and surpass most of the recently reported materials, highlighting $Gd_2B_2MoO_9$ as a promising candidate for next-generation cryogenic cooling applications.

Results

Structural features and multi-technique characterization of $Gd_2B_2MoO_9$ oxide

We fabricated the polycrystalline sample of $Gd_2B_2MoO_9$ oxide using a conventional solid-state reaction route. Its structure and phase purity were examined by powder X-ray diffraction (XRD) at room temperature (RT) and Rietveld refinement using Fullprof[38]. The resulting XRD profiles (Fig. 1a) show a reliable fit to a triclinic structure (space group $P1$). The refinement quality factors of R_B, R_{wp}, R_{exp} and χ^2 are all with reasonably low values of 3.85%, 5.04%, 3.07% and 2.69, respectively. The derived lattice parameters of a, b, c and α, β, γ are 5.201(1), 6.948(8), 10.321(2) Å and 73.987(2), 76.146(5), 72.626(4)°, respectively. More detailed, refined structural and refinement parameters are listed in Table S1. The low refinement parameter values confirm the single-phase nature of $Gd_2B_2MoO_9$ oxide.

Figure 1b, c illustrates the schematic structure and nearest-neighbor oxygen environments of Gd, B, and Mo. Two inequivalent Gd sites (Gd1 and Gd2) are each coordinated by eight O atoms, forming distorted GdO_8 hexagonal bipyramids (Fig. 1c1, 1c2). The Gd1–O and Gd2–O bond lengths are 2.159(5)–2.781(9) Å and 2.237(6)–2.675(8) Å, respectively. The Gd2–O–Gd2 bond angles range from 100.716(1)° to 115.010(1)°, while the Gd1–O–Gd1 angle is 100.851(0)°. The nearest Gd-Gd atoms form an isolated, slightly distorted, GF diamond lattice (Fig. 1b).

There are two inequivalent B sites (B1 and B2), each bonded in a trigonal planar geometry to three O atoms (Fig. 1c3, 1c4), with B1–O and B2–O bond lengths of 1.397(2)–1.593(1) Å and 1.353(2)–1.672(3) Å, respectively. The Mo atom is coordinated by four O atoms, forming MoO_4 tetrahedra (Fig. 1c5) with bond lengths of 1.559(3)–1.996(3) Å. Each GdO_8 bipyramid shares a corner with one MoO_4 tetrahedra and edges with three other GdO_8 bipyramids.

To comprehensively verify the chemical composition and structural features of $Gd_2B_2MoO_9$ oxide, we employed a combination of

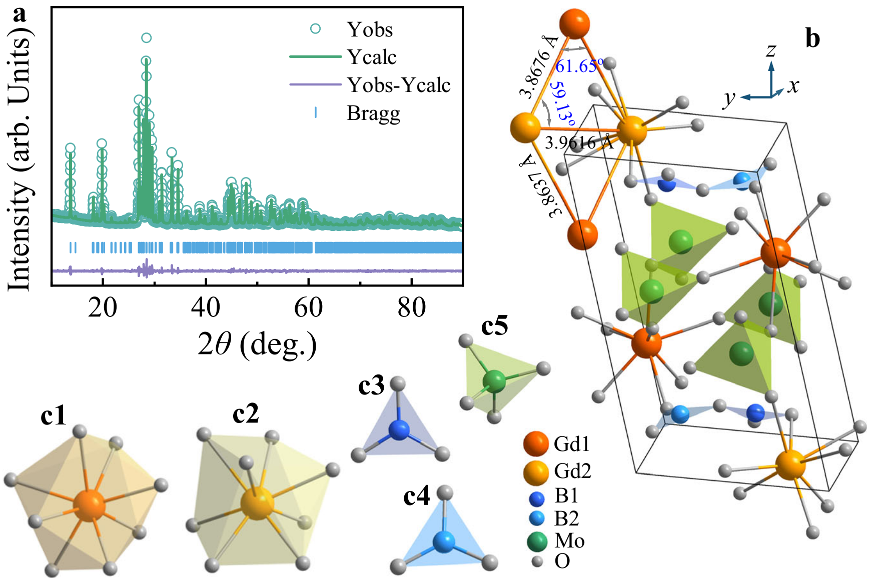

Fig. 1 | Structural features of $Gd_2B_2MoO_9$. **a** Experimental and Rietveld-refined powder X-ray diffraction (XRD) profiles indicate the high-quality of the studied sample. **b** Crystal structure diagram shows the formation of a geometrically frustrated (GF) diamond lattice by the nearest Gd-Gd atoms. **c1**–**c5** Local nearest oxygen coordination environments of Gd1, Gd2, B1, B2, and Mo atoms, respectively.

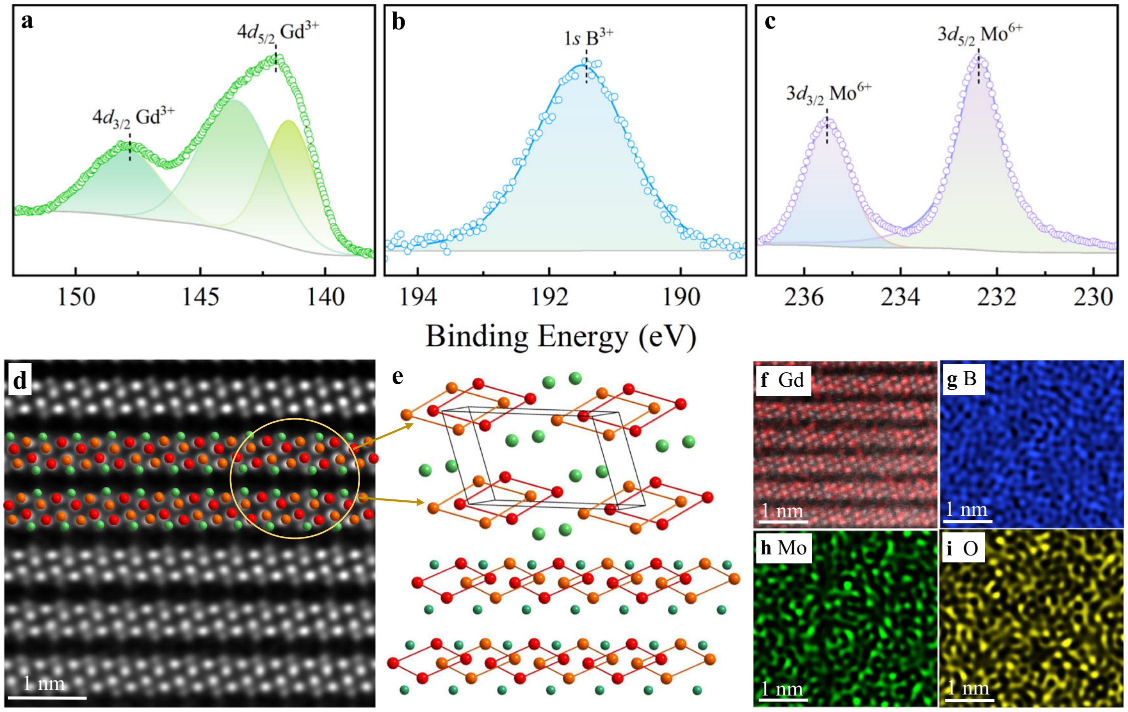

Fig. 2 | High-resolution XPS spectra and microstructural analysis of $Gd_2B_2MoO_9$. a–c Core-level XPS spectra and peak-fitting results for Gd, B, and Mo elements confirm the presence of Gd^{3+}, B^{3+}, and Mo^{6+} valence states. **d** High angle angular dark-field scanning transmission electron microscopy (HADDF-STEM) image proves the formation of geometrically frustrated (GF) diamond lattice by Gd-Gd atoms. **e** Schematic of the nearest Gd-Gd diamond lattice. Gd atoms are red, and Mo atoms are green. **f–i** Scanning transmission electron microscopy-based elemental energy-dispersive X-ray spectroscopy mapping.

spectroscopic and microscopic techniques. The chemical valence states of the constitute elements were determined by RT X-ray photoelectron spectroscopy (XPS). High-resolution core-level XPS spectra for Gd, B, and Mo, along with peak-fitting analyses (Fig. 2a–c), show that the experimental data agree well with the fitted results, confirming the presence of Gd^{3+}, B^{3+}, and Mo^{6+} in the oxide. Similar to those in recently reported Gd-containing oxides[23,35], the profile of $4\,d_{5/2}$ peak can be fitted by two components, demonstrates the existence of spin-orbit coupling interaction of 4*d* and 4 *f* electrons.

Morphology, chemical, and structural characteristics of $Gd_2B_2MoO_9$ oxide were further evaluated using scanning electron microscopy (SEM), high-resolution transmission electron microscopy (TEM), and scanning transmission electron microscopy (STEM) coupled with elemental energy-dispersive X-ray spectroscopy (EDS). The constituent elements of Gd, B, Mo and O elements are all uniformly distributed from the microscale to nanoscale (Figs. S1, S2) with the average atomic molar ratios of 15.3(3)%, 13.6(8)%, 7.2(2)% and 63.9(5)%, well-aligned with the nominal composition. The average particle size of $Gd_2B_2MoO_9$ oxide was determined to be 2.26(8) μm (Fig. S3). These SEM and TEM images, together with elemental EDS mappings, demonstrate the single-phase nature and good homogeneity of the present $Gd_2B_2MoO_9$ oxide.

An atom-resolved HAADF-STEM image and the corresponding EDS maps, acquired along the [111] zone axis (Figs. 2d, 2f-i), clearly resolve the Gd and Mo atomic columns. Four of the nearest Gd–Gd atoms, forming an isolated diamond lattice, are visible; the enlarged structural diagram (Fig. 2e) further confirms the Gd-dominated diamond-type GF structure of $Gd_2B_2MoO_9$ oxide.

First-principle insights into the ground state of $Gd_2B_2MoO_9$ oxide

To complement the experimental characterization, density functional theory (DFT) calculations were conducted to explore the magnetic and electronic properties of $Gd_2B_2MoO_9$ oxide in its ground state. Spin-polarized generalized gradient approximation (GGA) plus Hubbard U (GGA + U) approach with U_{eff} values up to 8 eV was performed using VASP software[39–41]. The magnetic ground state was firstly evaluated by computing the total energy (E_{tot}) for various constructed potential spin configurations, including non-magnetic (NM), ferromagnetic (FM), as well as three distinct antiferromagnetic (AFM) states, as illustrated in Fig. 3a–d. The derived values of E_{tot} for various potential magnetic structures with different U_{eff} values are all summarized in Table S2, in which the AFM configuration exhibits the lowest E_{tot} value, indicating that $Gd_2B_2MoO_9$ oxide favors an AFM ground state.

Further insights into the electronic structure were obtained by calculating the spin-polarized total density of states (DOS) and the atom-projected DOS for Gd (4 *f*), B (1 *s*), Mo (5 s), and O (2*p*) orbitals of $Gd_2B_2MoO_9$ oxide without and with different U_{eff} values up to 8 eV are illustrated in Figs. 3, S4, respectively. Both spin-majority and spin-minority channels in all the DOS are nearly identical, and a distinct band gap (BG) is observed at the Fermi level regardless of the U_{eff} values, confirming the AFM semiconductor nature of $Gd_2B_2MoO_9$ oxide. The total DOS is dominated by the Gd(4 *f*) partial DOS, with significant splitting observed, reflecting strong spontaneous polarization of the Gd^{3+} ions. The deduced BG value is 2.27(5) eV without U_{eff}, and it gradually rises to 2.43(8) eV with increasing U_{eff} up to 8 eV, as illustrated in Fig. S5. Moreover, the calculated average magnetic moments M_{cal} values range from 6.89(4) to 7.07(3) μ_B for Gd1, and from 6.91(3) to 7.06(5) μ_B for Gd2 atoms, respectively, closely matching the theoretical value for a free Gd^{3+} ion (7.0 μ_B).

Charge distribution and transfer characteristics were also analyzed using 2D maps and aerial view (Fig. 3f–h). O^{2-} ions share electrons with Gd^{3+}, B^{3+}, and Mo^{6+} ions, indicating a covalent bonding nature in $Gd_2B_2MoO_9$ oxide. Greater electronic overlap is observed between Mo^{6+} and O^{2-} atoms compared to Gd^{3+} and O^{2-} atoms. The aerial view reveals a positive peak for O^{2-} and a negative peak for B^{3+} atoms, while charges around Gd^{3+} atoms are well-localized, resulting in the large magnetic moments observed.

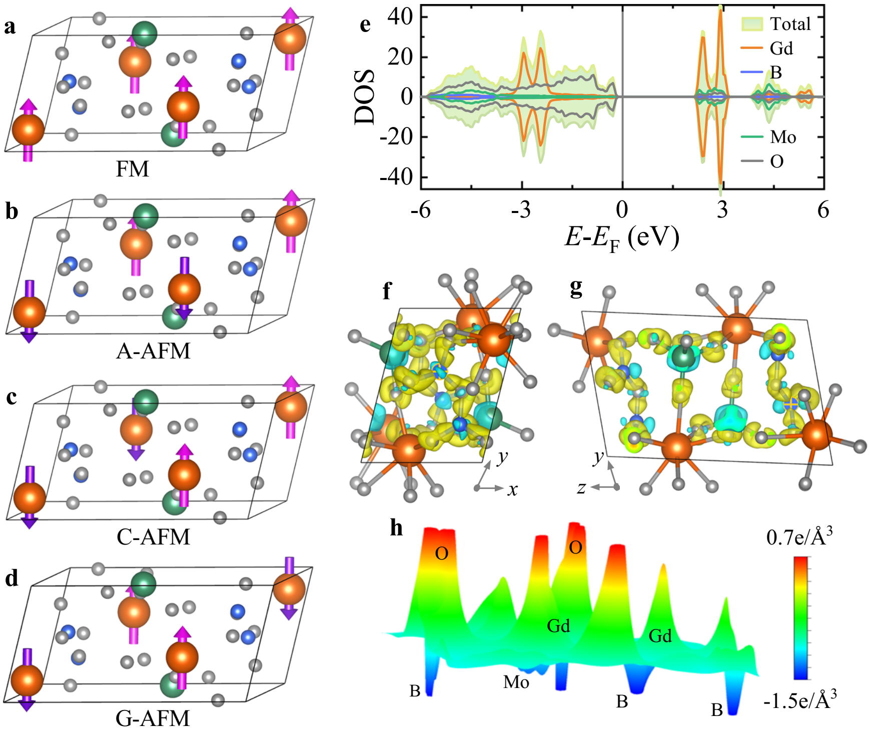

Fig. 3 | First-principles calculations for $Gd_2B_2MoO_9$. **a–d** Schematic representations of possible magnetic structures, including parallel (ferromagnetic, FM) and three typical anti-parallel (antiferromagnetic, AFM) states. Gd atoms are dark red, B atoms are blue, Mo atoms are green, and O atoms are gray. **e** Spin-polarized partial and total density of states (DOS) indicate a typical AFM semiconductor character and large spontaneous polarization of Gd^{3+} ions at the ground state. **f–h** Charge-density difference visualizations with 2D projections and aerial view show the localized charges around Gd^{3+} atoms.

Experimental determination of low-temperature magnetic and thermal properties of $Gd_2B_2MoO_9$

To comprehensively characterize the magnetic phase transition (MPT) and magnetic frustration properties of $Gd_2B_2MoO_9$ oxide, a series of magnetic and thermodynamic measurements was performed. The magnetic field (μ_0H) and temperature (T) dependent magnetization (M) were measured up to 5 T and down to 0.4 K. The T-dependent inverse magnetic susceptibility, $1/\chi$ ($\chi = M/\mu_0H$), under $\mu_0H = 1$ T, exhibits high-temperature linearity consistent with the Curie-Weiss (C–W) law (Fig. 4a), $\chi(T) = C/(T - \theta_P)$, wherein C and θ are the C-W constant and paramagnetic Curie temperature, respectively. Additionally, $C = N(\mu_B\mu_{eff})^2/3k_B$, wherein N is Avogadro's number, k_B is the Boltzmann constant, and μ_{eff} is the effective magnetic moment. Linear fitting above 6 K yields a negative θ_P of −3.11(5) K, indicative of AFM interactions at the ground state. This is further supported by the downturn in the χ_MT products at low temperatures (Fig. S6). The effective magnetic moment, μ_{eff}, is deduced to be 7.97(3) μ_B/Gd, closely matching the theoretical value of the free Gd^{3+} ion (7.94 μ_B).

Further insights were obtained from $\chi(T)$ measurements under field-cooled (FC) and zero-field-cooled (ZFC) protocols from 0.4 to 1.8 K with μ_0H values of 0.05, 0.2, and 0.5 T using a He-3 refrigerator (inset of Fig. 4a). Evidently, χ increases monotonously with decreasing T, peaking near its Néel temperature (T_N) of 0.79(5) K, before decreasing as T increases. These observations confirm the AFM ground state of $Gd_2B_2MoO_9$ oxide under low magnetic fields and align with DFT calculations. Whereas, under higher μ_0H of 0.5 T, χ increases monotonously with decreasing T and shows a saturation tendency at low temperatures, illustrating the occurrence of a field-induced metamagnetic transition from AFM ground state to ferromagnetic-like state. Additionally, the T-dependent χ_{ZFC} and χ_{FC} curves demonstrate high reversibility, which is advantageous for MR applications.

The T-dependent heat capacity, $C(T)$, was measured from 4 K down to 0.1 K under various magnetic fields (Fig. 4b). The existence of a pronounced $C(T)$ peak under zero-field and low magnetic fields demonstrates the long-range magnetic ordering in $Gd_2B_2MoO_9$ oxide, well-aligned with those by magnetic measurements and DFT calculations. The MPT temperature (T_N) was deduced to be 0.51(3) K from the inflection point in the temperature-dependent zero-field d(C/T)/dT curve (Fig. S7). The frustration parameter, $f = |\theta_P|/T_N$[30,33–35], was considered as a measurement of magnetic frustration level. Generally, no magnetic frustration when f value is lower than 1, whereas, being strong magnetic frustration if f was higher than 10[30,42]. For the present $Gd_2B_2MoO_9$ oxide, a f value of 6.1(4) has been obtained, which suggests a moderate magnetic frustration, favorable for ultra-low temperature MR[33–35]. At higher magnetic fields, only a broad peak is observed in $C(T)$, with the peak temperature increasing as μ_0H increases, consistent with magnetization results. The $M(\mu_0H)$ curve (Fig. 4c) at low temperatures shows that M increases rapidly at low μ_0H and saturates under high μ_0H above ~2.0 T. A nearly linear behavior in $M(\mu_0H)$ curves at high temperatures can be noted, consistent with the PM state. These findings corroborate DFT results, further confirming the dominate role of gadolinium in the magnetism of $Gd_2B_2MoO_9$ oxide.

Discussion

The MC performance of $Gd_2B_2MoO_9$ oxide was firstly assessed using $-\Delta S_M(T, \Delta\mu_0H)$ (Fig. 5a, b) calculated from $M(\mu_0H)$ (Fig. S8) and $C(T, \mu_0H)$ (Fig. 4b) data with the temperatures ranging from 0.5 to 10 K and 0.1 to 4 K, respectively. Subsequently, we estimated the relative cooling power (RCP) (Fig. S9) from the resulting $-\Delta S_M(T, \Delta\mu_0H)$ (Fig. 5a) data. The detailed calculation methods[43] are provided in the supplementary file. Although some differences in values exist, which are well within the intrinsic uncertainties documented by Pecharsky & Gschneidner[43], the $-\Delta S_M(T, \Delta\mu_0H)$ results from both approaches are consistent. The $-\Delta S_M$ value increases with decreasing temperature under each $\Delta\mu_0H$, reaches a maximum ($-\Delta S_M^{max}$), and then decreases.

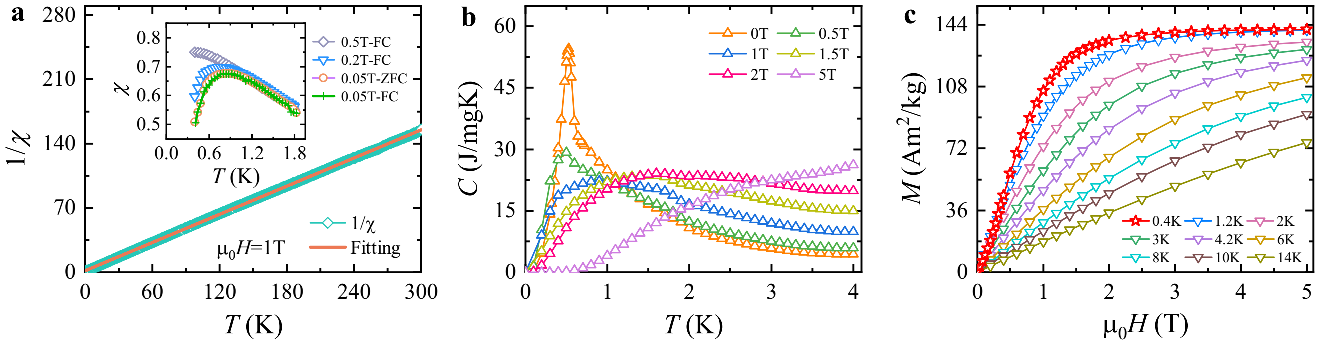

Fig. 4 | Magnetic and thermal properties of $Gd_2B_2MoO_9$. a Temperature dependence of inverse magnetic susceptibility $1/\chi$ (T) curves and Curie-Wiess fitting line under a magnetic field of 1 T; inset: Temperature dependence of magnetic susceptibility $\chi(T)$ curves under μ_0H of 0.05, 0.2 and 0.5 T by field-cooled (FC) and zero-field-cooled (ZFC) protocols demonstrating a typical antiferromagnetic ground state and a field-induced metamagnetic transition from antiferromagnetic to ferromagnetic-like state. **b** Temperature dependence of heat capacity $C(T)$ curves under different magnetic fields. **c** Magnetic field dependence of magnetization $M(\mu_0H)$ curves at several selected temperatures.

Under low $\Delta\mu_0H$ (0–0.5, 0–1, and 0–1.5 T), as temperature falls below ~0.5 K (Fig. 5b), the values of $-\Delta S_M$ change from positive to negative, indicating a transition from conventional to inverse MC effect, consistent with the AFM ground state inferred from magnetization and DFT results. In the section below, we use the ΔS_M results calculated from $M(\mu_0H)$ data for discussion and comparison since most of the reported results are also estimated by this method. Moreover, the $-\Delta S_M^{max}$ and *RCP* values all increase significantly with increasing $\Delta\mu_0H$ (Fig. S9), reaching 13.3, 33.7, and 55.0 J/kgK and 35.0, 113.9, and 378.5 J/kg under $\Delta\mu_0H$ = 0–1, 0–2, and 0–5 T, respectively. Despite the fact that these $-\Delta S_M^{max}$ and *RCP* values are still lower than several updated Gd-based metal-organic framework materials and divalent Eu-based oxides[24–28,44–46], the present $Gd_2B_2MoO_9$ oxide evidently has its own benefits of high density (5.76(5) g/cm^3), easy to be fabricated by a simple solid-state route, as well as good environmental stability.

For practical MR applications, minimizing system size is essential, making the volumes of MC materials and magnets critical factors. As such, evaluating the magnetic entropy change in volumetric terms ($-\Delta S_V$), expressed in the unit of mJ/cm^{3}K, under relatively low $\Delta\mu_0H$ (0–2 T) achievable by permanent magnets, is more suitable for assessing the MC performance of magnetic refrigerants. We therefore summarize the $-\Delta S^{max}$ values under $\Delta\mu_0H$ = 0–2 T, both per unit mass and per unit volume, for $Gd_2B_2MoO_9$ oxide, in comparison with commercial $Gd_3Ga_5O_{12}$ oxide and other recently reported ultra-low temperature MC materials[44–54] (Fig. 5c). While the mass-based $-\Delta S^{max}$ value of $Gd_2B_2MoO_9$ oxide under $\Delta\mu_0H$ = 0–2 T is lower than that of some reported materials[24–26], its volumetric $-\Delta S_V^{max}$ is approximately 1.88 times higher than commercial $Gd_3Ga_5O_{12}$ and exceeds most recently realized ultra-low temperature MC materials[27,28,46–53], positioning $Gd_2B_2MoO_9$ oxide among the leading ultra-low temperature magnetic refrigerants.

We further assessed the practical low-temperature cooling performances of $Gd_2B_2MoO_9$ oxide by direct measure its adiabatic demagnetization cooling $T(\mu_0H)$ curves (Fig. 6) using a custom-designed apparatus[6], with initial conditions and field control provided by a PPMS-9T system and by indirect calculation of adiabatic temperature change (ΔT_{ad}) below 4 K (inset of Fig. 6) from $C(T, \mu_0H)$ data, respectively. The resulting $T(\mu_0H)$ curves, starting from 9 T, for both $Gd_2B_2MoO_9$ and $Gd_3Ga_5O_{12}$ oxides at various initial temperature (T_o), exhibit three distinct stages: initially, the temperature decreases continuously with decreasing μ_0H and reaches a minimum temperature (T_{min}) at a critical field (μ_0H_{cr}); subsequently, the temperature increases slightly as the field is further reduced, indicating a transition from conventional to inverse MC effect. These behaviors are well consistent with those of indirectly calculated ΔT_{ad} (inset of Fig. 6) results, in which the values of ΔT_{ad} under low $\Delta\mu_0H$ clearly change from positive to negative around 0.71(3) K, further proving the AFM ground state. Additionally, the deduced ΔT_{ad} values by direct measurement method (marked by star) are well-aligned with those by indirectly calculated from $C(T, \mu_0H)$ data[43], as illustrated in the inset of Fig. 6. The values of T_{min} and μ_0H_{cr} of $Gd_2B_2MoO_9$ oxide are: 0.41 K and 0.62 T at T_O = 6 K; 0.28 K and 0.75 T at T_O = 4 K; 0.21 K and 0.84 T at T_O = 3 K; and 0.16 K and 1.04 T at T_O = 2 K, respectively. Under identical conditions, the T_{min} values are obviously lower than those of commercial $Gd_3Ga_5O_{12}$, making it promising for practical ultra-low temperature applications. Moreover, $Gd_2B_2MoO_9$ oxide can maintain the minimum temperature for more than half an hour (Fig. S10), demonstrating significant cooling capacity. It is worth noting that the achieved temperature of 0.16 K is well below the operating temperature (~1 K) of state-of-the-art silicon-based quantum computers[36,37], thereby enhancing the prospects for practical quantum computing applications. Additionally, $Gd_2B_2MoO_9$ oxide can be synthesized via a simple solid-state reaction route, and possess high chemical stabilities, high density, and environmental friendliness. These attributes underscore the potential of $Gd_2B_2MoO_9$ oxide as an excellent candidate for practical ultra-low temperature MR applications.

Methods

Sample synthesis

Polycrystalline $Gd_2B_2MoO_9$ oxide was fabricated by a solid-state reaction from high-purity (≥ 99.9 wt.%) $MgCO_3$, H_3BO_3, and $(NH_4)_6Mo_7O_{24}\cdot 4H_2O$ powders. The raw materials, weighted in stoichiometric proportions, were thoroughly ground by hand for 2 h with the addition of a small amount of alcohol to facilitate mixing. To compensate for the volatilization of H_3BO_3, a 6% excess was included to improve reproducibility. The mixture was preheated at 700 °C for 10 h. The resulting precursor was reground, pressed into thin pellets, and sintered in air at 900 °C for 18 h, followed by furnace cooling.

Microstructural characterization

The phase purity and crystal structure of $Gd_2B_2MoO_9$ oxide were examined by powder XRD at RT using a Rigaku-SmartLab diffractometer. The elemental chemical states were analyzed using XPS (Thermo-Scientific K-Alpha). The density was determined to be 5.76(5) g/cm^3 by Archimedes method. Microscopic morphology and EDS mapping were assessed using SEM (SM-7800F), TEM (FEI-TalosF200s), and STEM (FEI Titan-T300kV).

Physical property measurements

Magnetization measurements were acquired by a SQUID magnetometer (MPMS-Q3, Quantum Design) equipped with a ^{3}He refrigerator

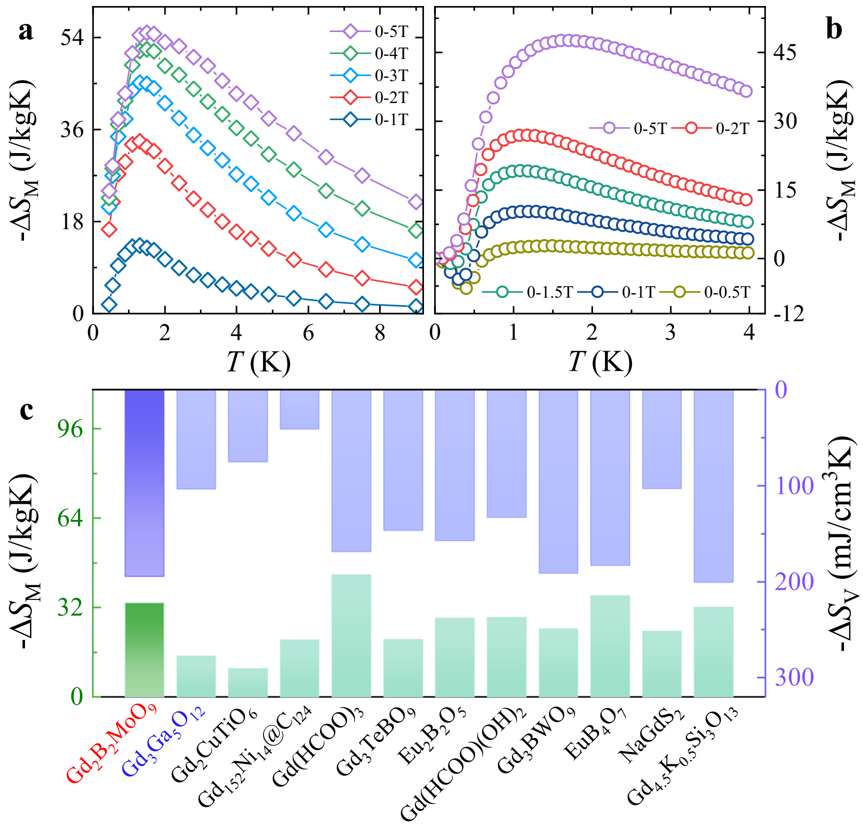

Fig. 5 | MC performance of $Gd_2B_2MoO_9$. Temperature dependence of magnetic entropy change $-\Delta S_M(T)$ derived from (**a**) $M(H)$ data and (**b**) $C(T)$ results. **c** Maximum volumetric entropy change $-\Delta S_V^{max}$ (light green column, left scale) and maximum mass entropy change $-\Delta S_M^{max}$ (light purple column, right scale) under $\Delta\mu_0 H = 0–2$ T, which are much larger than commercial ultra-low temperature magnetic refrigerant $Gd_3Ga_5O_{12}$ and surpass most of the benchmark ultra-low temperature magnetic refrigerants.

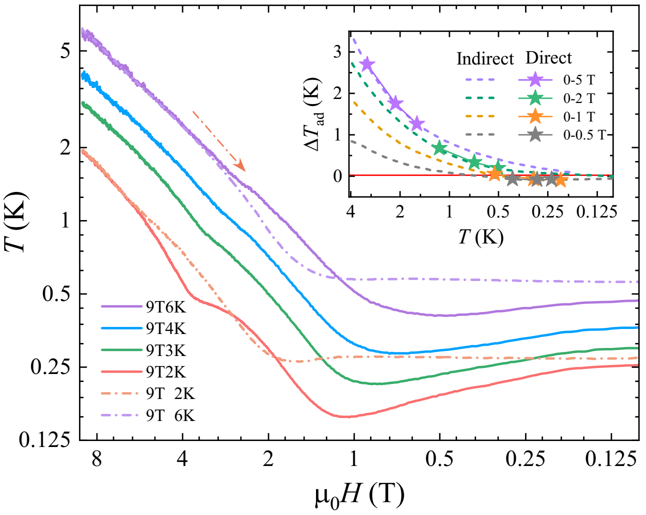

Fig. 6 | Practical low-temperature cooling performances of $Gd_2B_2MoO_9$. Direct measured the adiabatic demagnetization cooling $T(\mu_0 H)$ curves highlights a refrigeration down to 0.16 K, surpassing the commercial $Gd_3Ga_5O_{12}$ refrigerant. Inset presents temperature dependence of adiabatic temperature change $\Delta T_{ad}(T)$ curves by indirect calculation (dashed lines) and by direct measurement (marked by stars).

inset, using an irregular bulk sample with a mass of 3.65(4) mg. The field-dependent magnetization data used for the magnetic entropy change calculations were recorded during cooling and by incrementally measuring the field from 0 to 5 T. Specific heat measurements were performed using the adiabatic heat relaxation method with the PPMS-9T and a dilution refrigerator module; the sample mass in this case was 1.16(3) mg. All magnetic field-dependent addenda measurements were conducted under the magnetic fields of 0, 0.5, 1, 1.5, 2, and 5 T.

Calculation details

Atomic-level spin-polarized first-principles calculations were performed within the framework of DFT using commercial VASP software[39–41]. The valence electron contributions used [$5s^2$ $5p^6$ $4f^7$ $5d^1$ $6s^2$] for Gd, [$2s^2$ $3p^1$] for B, [$4d^5$ $5s^1$] for Mo, and [$2s^2$ $2p^4$] for O in the PAW pseudopotentials. The k-point mesh for $Gd_2B_2MoO_9$ oxide was set as $7 \times 5 \times 3$ using the Monkhorst-Pack method. Structural optimization of $Gd_2B_2MoO_9$ oxide was performed until the total energies and Hellman-Feynman forces on each atom were converged to below 0.01 eV/Å and 10^{-7} eV, respectively.

Quasi-adiabatic demagnetization device

The adiabatic demagnetization cooling $\mu_0 H(T)$ curves of $Gd_2B_2MoO_9$ oxide were determined using a custom-built apparatus[5], with initial conditions and field control provided by a PPMS-9T system. Approximately 3 g of powder sample was mixed with ~50 wt.% silver powder to enhance thermal conductivity and cold-pressed into a cylindrical pellet. Then, the sample pellet was mounted on a sapphire-plate holder, which was supported by a Vespel frame. A field-calibrated RuO_2 thermometer with the uncertainty less than 0.001 K was attached to the sample pellet for temperature measurements. The sample pellet was precooled to T_0 and stabilized in a chamber where residual gases were evacuated using a cryopump to ensure adiabatic conditions. The $\mu_0 H(T)$ curves were acquired by decreasing the external $\mu_0 H$ at a rate of 0.3 T/min from 9 to 0 T.

Data availability

The data that support the findings of this study are provided in the main text and the Supplementary Information. Source data are provided with this paper.

References

1. Xue, X. et al. CMOS-based cryogenic control of silicon quantum circuits. *Nature* **593**, 205–210 (2021).
2. Dong, M. et al. High-speed programmable photonic circuits in a cryogenically compatible, visible–near-infrared 200 mm CMOS architecture. *Nat. Photon.* **16**, 59–65 (2022).
3. Rowe, E. et al. Resonant enhancement of photo-induced superconductivity in K3C60. *Nat. Phys.* **19**, 1821–1826 (2023).
4. Pappalardo, R. T. et al. Science overview of the Europa Clipper mission. *Space Sci. Rev.* **220**, 40 (2024).
5. Xiang, J. S. et al. Giant magnetocaloric effect in spin supersolid candidate $Na_2BaCo(PO_4)_2$. *Nature* **625**, 270–275 (2024).
6. Zhu, P. et al. Emergent quantum Majorana metal from a chiral spin liquid. *Nat. Commun.* **16**, 2420 (2025).
7. Liebster, N. et al. Supersolid-like sound modes in a driven quantum gas. *Nat. Phys.* **21**, 1064–1070 (2025).
8. Cho, A. Helium-3 shortage could put the freeze on low-temperature research. *Science* **326**, 778–779 (2009).
9. Moya, X., Kar-Narayan, S. & Mathur, N. D. Caloric materials near ferroic phase transitions. *Nat. Mater.* **13**, 439–450 (2014).
10. Lin, J. C. et al. Colossal and reversible barocaloric effect in liquid-solid-transition materials n-alkanes. *Nat. Commun.* **13**, 596 (2022).
11. Klinar, K., Law, J. Y., Franco, V., Moya, X. & Kitanovski, A. Perspectives and energy applications of magnetocaloric, pyromagnetic, electrocaloric, and pyroelectric materials. *Adv. Energy Mater.* **14**, 2401739 (2024).
12. Zhang, Y. K. et al. Rare-Earth-Free $Mn_{30}Fe_{20-x}Cu_xAl_{50}$ magnetocaloric materials with stable cubic cscl-type structure for room-temperature refrigeration. *Adv. Funct. Mater.* **33**, 2310047 (2023).
13. Franco, V. et al. A. Magnetocaloric effect: from materials research to refrigeration devices. *Prog. Mater. Sci.* **93**, 112–232 (2018).
14. Debye, P. Einige Bemerkungen zur Magnetisierung bei tiefer Temperatur. *Ann. Phys.* **386**, 1154–1160 (1926).
15. Giauque, W. F. A thermodynamic treatment of certain magnetic effects. A proposed method of producing temperatures considerably below 1° absolute. *J. Am. Chem. Soc.* **49**, 1864–1870 (1927).
16. Giauque, W. F. & MacDougall, D. P. Attainment of temperatures below 1° absolute by demagnetization of $Gd_2(SO_4)_3{\cdot}8H_2O$. *Phys. Rev.* **43**, 768 (1933).
17. Barclay, J. A., Rosenblum, S. S. & Steyert, W. A. Low temperature thermal conductivity of some composite materials. *Cryogenics* **16**, 539–543 (1976).
18. Bulled, J. M. et al. Geometric frustration on the trillium lattice in a magnetic metal-organic framework. *Phys. Rev. Lett.* **128**, 177201 (2022).
19. Law, J. Y. & Franco, V. Modern rare-earth-containing magnetocaloric materials: Standing on the shoulders of giant $Gd_5Si_2Ge_2$. *Handbook on the Physics and Chemistry of Rare Earths* **64**, 175–246 (2023).
20. Zhang, Y. et al. Investigation of the structural and magnetic properties of the GdCoC compound featuring excellent cryogenic magnetocaloric performance. *Acta Mater.* **276**, 120128 (2024).
21. Zhong, H. et al. Design of excellent mechanical performances and magnetic refrigeration via in situ forming dual-phase alloys. *Adv. Mater.* **36**, 2402046 (2024).
22. Tang, X. et al. Magnetic refrigeration material operating at a full temperature range required for hydrogen liquefaction. *Nat. Commun.* **13**, 1817 (2022).
23. Chen, F. et al. Structural and magnetic characterization of weberite-type RE_3NbO_7 (RE = Gd, Dy, Ho and Er) ceramics featuring notable cryogenic magnetocaloric responses. *Sci. China Mater.* **68**, 2828–2840 (2025).
24. Xu, Q. et al. $Gd(OH)F_2$: a promising cryogenic magnetic refrigerant. *J. Am. Chem. Soc.* **144**, 13787–13793 (2022).
25. Ye, Z. X. et al. Coexistence of antiferromagnetic and ferromagnetic interactions in dimer-like arranged $EuAl_2O_4$ systems: regulatory strategy to giant low-field cryogenic magnetocaloric effects. *Adv. Funct. Mater.* 2509843 (2025).
26. Wang, B. J. et al. A record-high cryogenic magnetocaloric effect discovered in $EuCl_2$ compound. *J. Am. Chem. Soc.* **146**, 35016–35022 (2024).
27. Hamilton, A. C. S., Lampronti, G. I., Rowley, S. E. & Dutton, S. E. Enhancement of the magnetocaloric effect driven by changes in the crystal structure of Al-doped GGG, $Gd_3Ga_{5-x}Al_xO_{12}$ ($0 \le x \le 5$). *J. Phys.: Condens. Matt.* **26**, 116001 (2014).
28. Kleinhans, M. et al. Magnetocaloric properties of $R_3Ga_5O_{12}$ (R = Tb, Gd, Nd, Dy). *Phys. Rev. Appl.* **19**, 014038 (2023).
29. Bramwell, S. T. & Gingras, M. J. P. Spin ice state in frustrated magnetic pyrochlore materials. *Science* **294**, 1495–1501 (2001).
30. Gardner, J. S., Gingras, M. J. P. & Greedan, J. E. Magnetic pyrochlore oxides. *Rev. Mod. Phys.* **82**, 53 (2010).
31. Mukherjee, P. & Dutton, S. E. Enhanced magnetocaloric effect from cr substitution in ising lanthanide gallium garnets $Ln_3CrGa_4O_{12}$ (Ln = Tb, Dy, Ho). *Adv. Funct. Mater.* **27**, 1701950 (2017).
32. Li, H. et al. Magnetocaloric effect of topological excitations in Kitaev magnets. *Nat. Commun.* **15**, 7011 (2024).
33. Zhitomirsky, M. E. Enhanced magnetocaloric effect in frustrated magnets. *Phys. Rev. B* **67**, 104421 (2003).
34. Koskelo, E. A. C. et al. Comparative Study of magnetocaloric properties for Gd^{3+} compounds with different frustrated lattice geometries. *PRX Energy* **2**, 033005 (2023).
35. Zhang, Y., Hao, W., Lin, J., Li, H. F. & Li, L. Geometrically frustrated $Gd_2Ti_2O_7$ oxide: a comprehensive exploration of structural, magnetic, and magnetocaloric properties for cryogenic magnetic cooling applications. *Acta Mater* **272**, 119946 (2024).
36. Yang, C. H. et al. Operation of a silicon quantum processor unit cell above one kelvin. *Nature* **580**, 350–354 (2020).
37. Noah, G. M. et al. CMOS on-chip thermometry at deep cryogenic temperatures. *Appl. Phys. Rev.* **11**, 021414 (2024).
38. Rodriguez-Carvajal, J. FULLPROF: a Rietveld and pattern-matching analysis program. Laboratoire Léon Brillouin CEA-CNRS, France (2007).
39. Perdew, J., Burke, K. & Ernzerhof, M. Generalized gradient approximation made simple. *Phys. Rev. Lett.* **77**, 3865 (1996).
40. Evarestov, R. A. & Smirnov, V. P. Modification of the Monkhorst-Pack special points meshes in the Brillouin zone for density functional theory and Hartree-Fock calculations. *Phys. Rev. B* **70**, 233101 (2004).
41. Kresse, G. & Furthmüller, J. Efficient iterative schemes for ab initio total-energy calculations using a plane-wave basis set. *Phys. Rev. B* **54**, 11169 (1996).
42. Ramirez, A. P. Strongly geometrically frustrated magnets. *Annu. Rev. Mater. Sci.* **24**, 453–480 (1994).
43. Pecharsky, V. K. & Gschneidner, K. A. Jr. Magnetocaloric effect from indirect measurements: magnetization and heat capacity. *J. Appl. Phys.* **86**, 565–575 (1999).
44. Tziotzi, T. G. et al. A $\{Gd_{12}Na_6\}$ molecular quadruple-wheel with a record magnetocaloric effect at low magnetic fields and temperatures. *J. Am. Chem. Soc.* **145**, 7743–7747 (2023).
45. Wang, Y. P. et al. Giant low-field cryogenic magnetocaloric effect in a polycrystalline EuB_4O_7 compound. *J. Am. Chem. Soc.* **146**, 3315–3322 (2024).

46. Xu, N., Chen, W. M., Ding, Y. S. & Zheng, Z. P. A cubic Tinkertoy-like heterometallic cluster with a record magnetocaloric effect. *J. Am. Chem. Soc.* **146**, 9506–9511 (2024).
47. Zhang, Y. K., Na, Y. Z., Hao, W. X., Gottschall, T. & Li, L. W. Enhanced cryogenic magnetocaloric effect from 4*f*-3*d* exchange interaction in *B*-Site ordered Gd_2CuTiO_6 double perovskite oxide. *Adv. Funct. Mater.* **34**, 2409061 (2024).
48. Lorusso, G. et al. A dense metal-organic framework for enhanced magnetic refrigeration. *Adv. Mater.* **25**, 4653–4656 (2013).
49. Zhou, C. Q. & Li, R. K. Gd_3TeBO_9: a rare-earth borate with significant magnetocaloric effect. *Chem. Eur. J.* **30**, e202303048 (2024).
50. Yang, Z. Y. et al. Large magnetocaloric effect in gadolinium borotungstate Gd_3BWO_9. *J. Mater. Chem. C.* **8**, 11866 (2020).
51. Mo, Z. J. et al. Magnetic properties and large low-field cryogenic magnetocaloric effect in the divalent europium borate $Eu_2B_2O_5$ compound. *Mater. Today Phys.* **41**, 101351 (2024).
52. Delacotte, C. et al. $NaGdS_2$: a promising sulfide for cryogenic magnetic cooling. *Chem. Mater.* **34**, 1829–1837 (2022).
53. Xu, Q. F. et al. Enhancing the performance of magnetic refrigerants through tuning their magnetism from antiferromagnetism to weak ferromagnetism. *Sci. China Mater.* **65**, 3171–3174 (2022).
54. Zhang, Y. K., Li, A. S., Hao, W. X., Li, H. F. & Li, L. W. Apatite-type gadolinium-based dense $MGd_4Si_3O_{13}$ (M = Mg, Ca, Sr) ceramics: an emerging class of sub-liquid helium temperature magnetic refrigerant. *Acta Mater.* **292**, 121033 (2025).

Acknowledgments

The present work was supported by the National Natural Science Foundation of China (Grant Nos. 52472274 L.W.L. and 52572290 Y.K.Z.) and Zhejiang Provincial Natural Science Foundation of China (Grant No. LZ25E020002 Y.K.Z.). The authors of L.W.L. and Y.K.Z. also acknowledge Dr. Chao Zhang from the Instrumentation and Service Center for Physical Sciences at Westlake University for the magnetization measurements and the Supercomputing Center of Hangzhou Dianzi University for providing computing resources.

Author contributions

Y.K.Z., X.F.Z., and L.W.L. raised the idea. L.W.L., H.F.L., P.J.S., and S.Q.Z. conceived the experiments. F.Y.C. and Y.K.Z. synthesized and characterized the sample. Y.Z.N., L.W.L., and Y.K.Z. performed the magnetization measurements and DFT calculations. X.Y.L. and J.S.X. performed the Quasi-Adiabatic Demagnetization measurements. All authors participated in the data analysis and manuscript preparation.

Competing interests

The authors declare no competing interests.

Additional information

Supplementary information The online version contains supplementary material available at https://doi.org/10.1038/s41467-025-68278-z.

Correspondence and requests for materials should be addressed to Lingwei Li.

Peer review information *Nature Communications* thanks Sagar Ghorai and the other anonymous reviewer(s) for their contribution to the peer review of this work. A peer review file is available.